Monthly Notices
of the
ROYAL ASTRONOMICAL SOCIETY

MNRAS **531,** 2148–2161 (2024)
https://doi.org/10.1093/mnras/stae1304
Advance Access publication 2024 May 20

Quantum refraction effects in pulsar emission

Dong-Hoon Kim ,[1,2★] Chul Min Kim[3] and Sang Pyo Kim[4,5]

[1] *The Research Institute of Basic Science, Seoul National University, Seoul 08826, Republic of Korea*
[2] *Department of Physics and Astronomy, Seoul National University, Seoul 08826, Republic of Korea*
[3] *Advanced Photonics Research Institute, Gwangju Institute of Science and Technology, Gwangju 61005, Republic of Korea*
[4] *Department of Physics, Kunsan National University, Gunsan 54150, Republic of Korea*
[5] *Asia Pacific Center for Theoretical Physics, Pohang 37673, Republic of Korea*

Accepted 2024 May 13. Received 2024 April 18; in original form 2024 January 6

ABSTRACT

Highly magnetized neutron stars exhibit the vacuum non-linear electrodynamics effects, which can be well-described using the one-loop effective action for quantum electrodynamics. In this context, we study the propagation and polarization of pulsar radiation, based on the post-Maxwellian Lagrangian from the Heisenberg–Euler–Schwinger action. Given the refractive index obtained from this Lagrangian, we determine the leading-order corrections to both the propagation and polarization vectors due to quantum refraction via perturbation analysis. In addition, the effects on the orthogonality between the propagation and polarization vectors and the Faraday rotation angle, all due to quantum refraction are investigated. Furthermore, from the dual refractive index and the associated polarization modes, we discuss quantum birefringence, with the optical phenomenology analogous to its classical counterpart.

Key words: magnetic fields – pulsars emissions – non-linear electrodynamics – post-Maxwellian Lagrangian model – quantum refraction – quantum birefringence.

1 INTRODUCTION

Neutron stars have strong magnetic fields on their surface from 10^8 G up to 10^{15} G, and in particular magnetars have the strongest magnetic fields in the Universe with 10^{13}–10^{15} G, which are near or a little above the supercritical value $B_{\rm c} = m_{\rm e}^2 c^3/e\hbar = 4.4 \times 10^{13}$ G (Olausen & Kaspi 2014; Kaspi & Beloborodov 2017). In such strong magnetic fields, the vacuum becomes a polarized medium due to the interaction of the fields with virtual electron–positron pairs. As a consequence, a photon propagating in the strong magnetic field background can be refracted or split, which is prohibited in the classical Maxwell theory.

The critical magnetic field (or the so-called Schwinger field) is three order higher than the current highest strength achieved with ultra-intense lasers; i.e. $B = 4.9 \times 10^{-4} B_{\rm c}$ (Yoon et al. 2021). Therefore, highly magnetized neutron stars will provide a celestial laboratory to test quantum electrodynamics (QED) in the strong field regime and the relevant consequences (for review and references, see Ruffini, Vereshchagin & Xue 2010; Fedotov et al. 2023; Hattori, Itakura & Ozaki 2023). Recently, the surface magnetic field for *Swift* J0243.6+6124 has been directly measured from the detection of cyclotron resonance scattering (Kong et al. 2022). Also, space missions have been proposed to investigate the strong-field QED effects: the enhanced X-ray Timing and Polarimetry (eXTP; Santangelo et al. 2019) and the Compton Telescope project (Wadiasingh et al. 2019).

In this paper, we study the propagation and polarization of a photon in the dipole magnetic field background of a pulsar model, based on the post-Maxwellian (PM) Lagrangian; it is, in the weak-field limit, the generic form of non-Maxwellian Lagrangian for the non-linear vacuum (Sorokin 2022) and has been used to test vacuum polarization effects in the PVLAS (Polarizzazione del Vuoto con LAser) project (Ejlli et al. 2020). The Heisenberg–Euler–Schwinger (HES) Lagrangian of strong-field QED (Heisenberg & Euler 1936; Schwinger 1951) is also well-approximated by the PM Lagrangian below the critical field strength. Here, we develop the recent analysis of vacuum birefringence in Kim & Kim (2023) further for a practical model of pulsar emission, where the magnetic field is defined for an oblique rotator with an inclination angle and the electric field is discarded. We consider the dual refractive index and the associated polarization vectors of a probe photon (Kim & Kim 2022) to investigate the photon propagation in the strong magnetic field background of this pulsar model. Then the leading-order corrections to both the propagation and polarization vectors due to quantum refraction are determined via perturbation analysis. Our study provides a novel, complementary approach to and an elaboration of other similar studies in Heyl & Shaviv (2000, 2002), Heyl, Shaviv & Lloyd (2003), Caiazzo & Heyl (2018, 2021), Heyl & Caiazzo (2018), Caiazzo (2019), Caiazzo et al. (2022).

★ E-mail: ki13130@gmail.com

The paper is organized as follows. In Section 2, we review the Lagrangian formalism for the non-linearity of the quantum vacuum due to strong electromagnetic fields; a brief account of the HES Lagrangian and the PM Lagrangian as its approximation is given. In Section 3, we work out the deflection of a light ray from pulsar emission due to quantum refraction; the leading-order corrections to the propagation vector and then to the trajectory of the light ray are determined. In Section 4, we look into the dual refractive index and the associated polarization modes of the light ray under the effect of quantum refraction; the leading-order corrections to the polarization vectors for Case I (Section 4.1) and Case II (Section 4.2) are determined. In addition, the effects on the orthogonality between the propagation and polarization vectors and the Faraday rotation angle, due to quantum refraction are investigated. Furthermore, in regard to the optical phenomenology from the dual refractive index and the associated polarization modes, we discuss quantum birefringence for this pulsar emission. Then finally, we conclude the paper with discussions on other similar studies and follow-up studies.

2 NON-LINEAR ELECTRODYNAMICS DUE TO STRONG FIELDS

Non-linear electrodynamic (NED) effects of the vacuum in the presence of strong electromagnetic fields have been studied employing the *effective Lagrangian* formalism. One of the most well-known NED models is the HES Lagrangian, which is obtained by adding the one-loop QED correction to the Maxwell Lagrangian, due to spin-1/2 fermions of mass m_{e} and charge e in electromagnetic fields of arbitrary strengths (Heisenberg & Euler 1936; Schwinger 1951): in the convention with $\hbar = c = 1$,

$$\mathcal{L}_{\mathrm{HES}}\left(a, b\right) = \mathcal{L}^{(0)}\left(a, b\right) + \mathcal{L}^{(1)}\left(a, b\right) = \frac{b^2 - a^2}{2} + \mathcal{L}^{(1)}\left(a, b\right), \tag{1}$$

where $\mathcal{L}^{(0)}\left(a, b\right)$ refers to the classical Maxwell Lagrangian, defined through

$$a \equiv \sqrt{\sqrt{F^2 + G^2} + F}, \; b \equiv \sqrt{\sqrt{F^2 + G^2} - F}, \tag{2}$$

with the Lorentz- and gauge-invariant Maxwell scalar F and pseudo-scalar G

$$F \equiv \frac{1}{4} F^{\mu\nu} F_{\mu\nu} = \frac{1}{2}\left(\mathbf{B}^2 - \mathbf{E}^2\right) = \frac{1}{2}\left(a^2 - b^2\right), \; G \equiv \frac{1}{4} F^{\mu\nu} F^{*}_{\mu\nu} = -\mathbf{E}\cdot\mathbf{B} = \mathrm{sign}\left(\pm\right) ab, \tag{3}$$

and $\mathcal{L}^{(1)}\left(a, b\right)$ refers to the Lagrangian of one-loop correction,

$$\mathcal{L}^{(1)}\left(a, b\right) = -\frac{1}{8\pi^2}\int_0^{\infty} \mathrm{d}s \, \frac{e^{-m_{\mathrm{e}}^2 s}}{s^3}\left\{\left(eas\right)\coth\left(eas\right)\left(ebs\right)\cot\left(ebs\right) - \left[1 + \frac{\left(eas\right)^2 - \left(ebs\right)^2}{3}\right]\right\}. \tag{4}$$

However, in the weak-field limit (below the critical field strength B_{c}), the HES Lagrangian (1) has the leading-order contribution, the so-called post-Maxwellian (PM) Lagrangian (Euler & Kockel 1935):[1]

$$\mathcal{L}_{\mathrm{PM}}\left(a, b\right) = -F + \eta_1 F^2 + \eta_2 G^2, \tag{5}$$

where η_1 and η_2 are parameters defined via $\eta_1/4 = \eta_2/7 = e^4/\left(360\pi^2 m_{\mathrm{e}}^4\right)$.

In some NED models, a parity violating term proportional to FG is added to the PM Lagrangian (Ni, Mei & Wu 2013). However, for the rest of this paper, our analysis is based on the PM Lagrangian; the dual refractive index as given by equation (9) in Section 3 is derived using this (Adler 1971; Kim & Kim 2022).

3 DEFLECTION OF A LIGHT RAY DUE TO QUANTUM REFRACTION

A light ray is defined as an orthogonal trajectory to the geometrical wavefront $\mathcal{S}\left(x, y, z\right) = \mathrm{const.}$, and therefore can be described by

$$n\frac{\mathrm{d}\mathbf{r}}{\mathrm{d}s} = \nabla\mathcal{S}, \tag{6}$$

where s is an affine parameter to measure the length of the ray and $n = n(\mathbf{r})$ is the refractive index given as a function of the position $\mathbf{r}$ on the ray (Born et al. 1999). It can be further shown that

$$\frac{\mathrm{d}}{\mathrm{d}s}\left(n\frac{\mathrm{d}\mathbf{r}}{\mathrm{d}s}\right) = \nabla n. \tag{7}$$

Let $\hat{\mathbf{n}} \equiv \mathrm{d}\mathbf{r}/\mathrm{d}s$ be the unit propagation vector for the light ray emitted from a spot either at rest or in motion at a constant velocity.[2] Then equation (7) leads to (Born et al. 1999)

$$\hat{\mathbf{n}} = \begin{cases} \mathrm{const.} & \text{for } n = \mathrm{const.}, \\ \frac{\int \nabla n \, \mathrm{d}s}{n} & \text{for } n \neq \mathrm{const.}. \end{cases} \tag{8}$$

---

[1] In effect, the PM Lagrangian approximates the HES Lagrangian well even up to $B = 0.14B_{\mathrm{c}}$, with an error less than 1 per cent.

[2] This is in contrast with our actual case, wherein the emission spot itself is under the centrifugal acceleration due to the rotation of a pulsar magnetosphere, as described by equation (13).

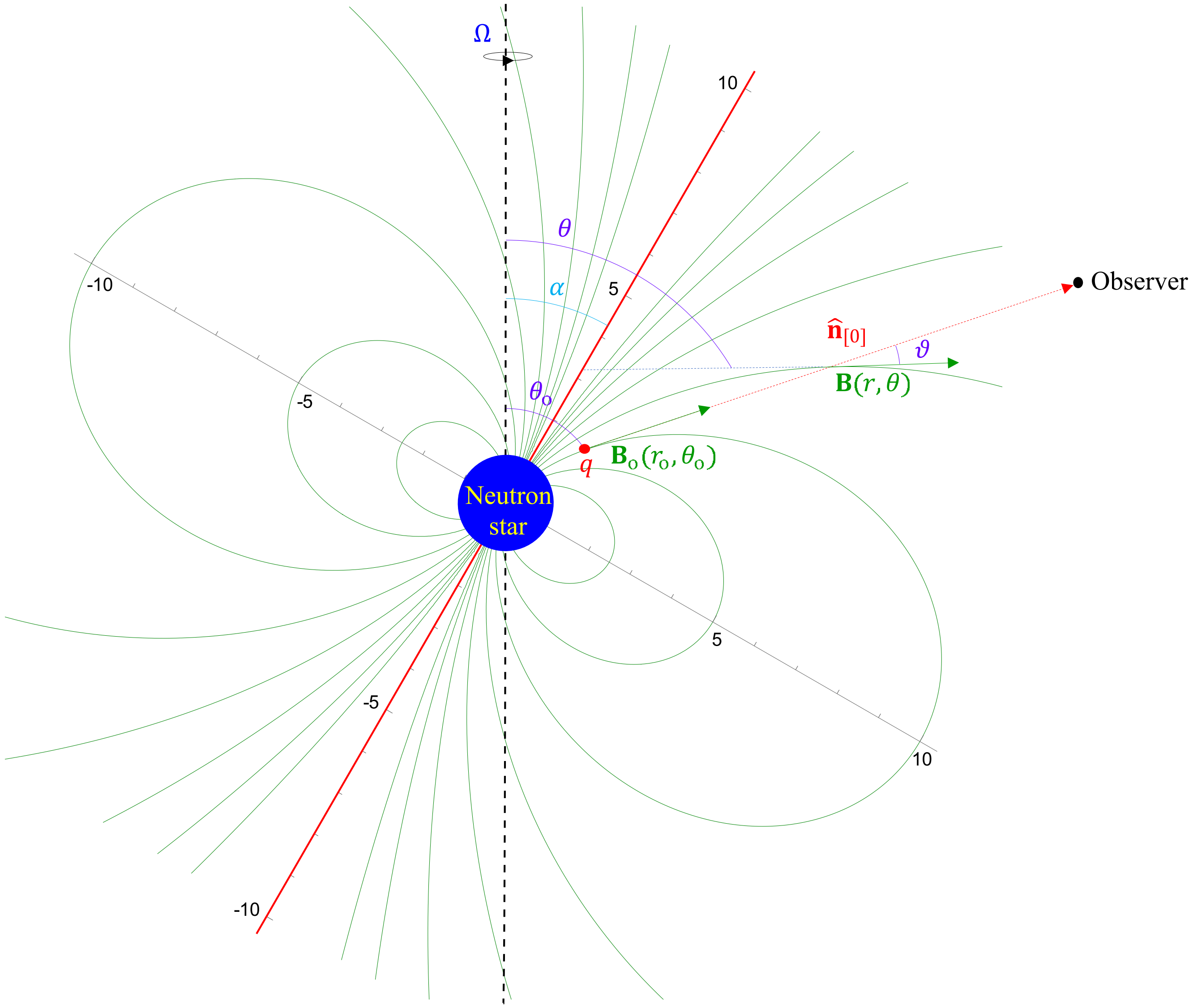

Figure 1. A cross-sectional view of a pulsar magnetosphere with the dipole magnetic field lines (green) around a neutron star. The vertical dashed line (black) and the inclined solid line (red) represent the rotation axis and the magnetic axis, respectively. α between these axes denotes the inclination angle. The scale of the unity in this graph is equivalent to the neutron star radius $\sim 10^6$ cm. The red dotted line represents the trajectory curve of the light ray traced by $\hat{\mathbf{n}}_{[0]}$ as projected on to the xz-plane. (Credit: Kim & Trippe 2021, reproduced with modifications.)

The expression of $\hat{\mathbf{n}}$ for $n \neq$ const. can be applied to a mechanism of how the light ray is deflected, for example due to the quantum refraction effect in pulsar emission, as will be described below. In the presence of the effect, the refractive index n is given by a function of the position $\mathbf{r}$, at which the light ray crosses a local magnetic field line in a pulsar magnetosphere; otherwise, it would simply be a constant.

According to Kim & Kim (2022), the refractive index n can be derived using the PM Lagrangian (5) as

$$n = \begin{cases} \sqrt{\frac{1-(\eta_1-2\eta_2)B^2}{1-(\eta_1-2\eta_2\cos^2\vartheta)B^2}} & \text{for Case I,} \\ \sqrt{\frac{1-\eta_1 B^2}{1-(\eta_1+2\eta_1\sin^2\vartheta)B^2}} & \text{for Case II,} \end{cases} \tag{9}$$

where B is the local magnetic field strength at a point in a pulsar magnetosphere, and ϑ denotes the angle between the light ray trajectory and the local magnetic field line (see Fig. 1). Here, we have named Case I and Case II for two different values of the refractive index attributed to the same point in the magnetosphere; the propagation and polarization of the light ray are associated with these values. Later in Sections 4.1 and 4.2, the two polarization vectors for Case I and Case II, as given by (41) and (50), respectively are set to be orthogonal to each other and to the propagation vector such that the three vectors form a classical orthonormal basis. However, for the rest of this section, we focus on Case I as there is little difference in the propagation of the light ray between the two cases. Then in Section 4, we look into the polarization of the light ray for both the cases and discuss quantum birefringence in relation to it.

One should note that the refractive index n as given by (9) has no dependence on the frequency of radiation. Consequently, in our entire analysis, the quantum refraction effects derived from this, on the propagation and polarization of a photon have no frequency dependence either, as can be checked with equations (11) and (40), respectively later. However, in order for equation (9) to be considered valid, the frequency of pulsar radiation must be significantly lower than that for excitation of the quantum vacuum ($\sim 10^{20}$ Hz; in the gamma-ray regime), which corresponds to the photon energy required to create an electron–positron pair, such that the vacuum is far from resonance. In addition, the plasma effects may be neglected if the pulsar radiation frequency is much higher than the local plasma frequency ($\sim 10^9$ Hz; Petri 2016). Therefore, our pulsar radiation can be safely assumed to cover optical to X-ray emissions ($\sim 10^{12}$ to 10^{17} Hz) in this work.

One can expand the refractive index n for Case I in equation (9), having η_1, $\eta_2 \sim 10^{-31}\,\mathrm{g}^{-1}\,\mathrm{cm}\,\mathrm{s}^2$, and $B < B_\mathrm{c}$ (critical magnetic field) $\sim 10^{13}$ G, and thus $\eta_1 B^2$, $\eta_2 B^2 \ll 1$. Then it can be approximated as (Adler 1971)

$$n \approx 1 + \eta_2 B^2 \sin^2\vartheta + \mathcal{O}\left(\eta_1^2 B^4, \eta_1\eta_2 B^4, \eta_2^2 B^4\right), \tag{10}$$

which implies that the term $\eta_2 B^2 \sin^2\vartheta \sim 10^{-4}(B/B_\mathrm{c})^2$ is the leading order quantum correction to $n = 1$ for classical optics, while $\mathcal{O}\left(\eta_1^2 B^4, \eta_1\eta_2 B^4, \eta_2^2 B^4\right)$ means the next-to-leading order terms to be ignored in our analysis. For computational purposes, the correction can be treated as the leading order perturbation with $\eta_2 B^2$ being a perturbation parameter. It should be noted here that $n \to 1$, i.e. the refractive index goes back to the classical limit as $B \to 0$ in the far field zone of the magnetosphere.

Keeping equation (10) in mind, from equation (8) one can determine the deflection of the light ray to leading order via

$$\delta\hat{\mathbf{n}}_{[1]} \approx \int \nabla\delta n_{[1]}\,\mathrm{d}s + \mathcal{O}\left(_{[2]}\right), \tag{11}$$

where $\delta(\cdots)_{[1]}$ means the leading order quantum correction to the quantity $(\cdots)$, led by $\eta_1 B^2$ or $\eta_2 B^2$, and $\mathcal{O}\left(_{[2]}\right)$ is a shorthand expression for $\mathcal{O}\left(\eta_1^2 B^4, \eta_1\eta_2 B^4, \eta_2^2 B^4\right)$. On the other hand, by $\hat{\mathbf{n}}_{[0]}$ we mean the *unperturbed* (classical) propagation direction of the light ray. A classical trajectory of the light ray traced by $\hat{\mathbf{n}}_{[0]}$ is as represented by the red dashed line as in Fig. 1, wherein it appears to be a straight line, being projected on to the xz-plane.

In our pulsar emission model, a light ray of curvature radiation is emitted from the dipole magnetic field:

$$\mathbf{B}(r,\theta,\phi) = \frac{2\mu\,(\cos\alpha\cos\theta + \sin\alpha\sin\theta\cos\phi)}{r^3}\mathbf{e}_{\hat{r}} + \frac{\mu\,(\cos\alpha\sin\theta - \sin\alpha\cos\theta\cos\phi)}{r^3}\mathbf{e}_{\hat{\theta}} + \frac{\mu\sin\alpha\sin\phi}{r^3}\mathbf{e}_{\hat{\phi}}, \tag{12}$$

where μ is the magnetic dipole moment, α denotes the inclination angle between the rotation axis and the magnetic axis, and the light ray is tangent to the field line at the emission point $(x_\mathrm{o}, y_\mathrm{o}, z_\mathrm{o}) = (r_\mathrm{o}\sin\theta_\mathrm{o}, 0, r_\mathrm{o}\cos\theta_\mathrm{o})$ (see Fig. 1). At the same time, however, our pulsar magnetosphere rotates, and the magnetic field lines get twisted due to the magnetocentrifugal acceleration on the plasma particles moving along the field lines (Blandford & Payne 1982). Taking into consideration this magnetohydrodynamic (MHD) effect due to rotation, one can describe classically the propagation direction of the light ray, which must line up with the particle velocity in order for an observer to receive the radiation, as (Gangadhara 2005)

$$\hat{\mathbf{n}}_{[0]} = \beta\hat{\mathbf{B}} + \frac{\boldsymbol{\Omega}\times\mathbf{r}}{c}, \tag{13}$$

where on the right-hand side $\hat{\mathbf{B}} \equiv \mathbf{B}/|\mathbf{B}|$ and the second term accounts for the centrifugal acceleration, with $\boldsymbol{\Omega} \equiv \Omega\mathbf{e}_z$ and Ω being a pulsar rotation frequency, and

$$\beta \equiv \left[1 - \left(\frac{\Omega r}{c}\right)^2 \sin^2\theta\left(1 - \frac{\sin^2\alpha\sin^2\phi}{3\cos^2\theta' + 1}\right)\right]^{1/2} - \frac{\Omega r}{c}\frac{\sin\alpha\sin\theta\sin\phi}{\left(3\cos^2\theta' + 1\right)^{1/2}}, \tag{14}$$

with c being the speed of light and $\cos\theta' \equiv \cos\alpha\cos\theta + \sin\alpha\sin\theta\cos\phi$.

However, during the rotation the azimuthal phase changes by $\phi \sim \Omega t$, while our light ray has propagated a distance by $s \sim ct$. We describe the propagation of the light ray with the consideration of the MHD effect above, assuming ϕ to be very small; e.g. $\phi \lesssim 10^{-1}$ is considered for a millisecond pulsar with $\Omega \sim 10^2$ Hz, during the time of rotation $t \lesssim 10^{-3}$ s, such that $s \lesssim 10^7$ cm, which corresponds to the propagation distance within about 10 times the neutron star radius. Then, for equation (13), we take only the leading order expansions of $\hat{\mathbf{B}}(r_\mathrm{o}, \theta_\mathrm{o}, \phi)$ and $\beta(r_\mathrm{o}, \theta_\mathrm{o}, \phi)$ in ϕ from equations (12) and (14), respectively, and obtain $\hat{\mathbf{n}}_{[0]} = \hat{n}_{x[0]}\mathbf{e}_x + \hat{n}_{y[0]}\mathbf{e}_y + \hat{n}_{z[0]}\mathbf{e}_z$, expressed in Cartesian coordinates:

$$\hat{n}_{x[0]} \approx \frac{2\cos(\theta_\mathrm{o} - \alpha)\sin\theta_\mathrm{o} + \sin(\theta_\mathrm{o} - \alpha)\cos\theta_\mathrm{o}}{\left(3\cos^2(\theta_\mathrm{o} - \alpha) + 1\right)^{1/2}} + \mathcal{O}\left(\phi^2, (\Omega r_\mathrm{o}/c)^2, \phi\,(\Omega r_\mathrm{o}/c)\right), \tag{15}$$

$$\hat{n}_{z[0]} \approx \frac{2\cos(\theta_\mathrm{o} - \alpha)\cos\theta_\mathrm{o} - \sin(\theta_\mathrm{o} - \alpha)\sin\theta_\mathrm{o}}{\left(3\cos^2(\theta_\mathrm{o} - \alpha) + 1\right)^{1/2}} + \mathcal{O}\left(\phi^2, (\Omega r_\mathrm{o}/c)^2, \phi\,(\Omega r_\mathrm{o}/c)\right), \tag{16}$$

and

$$\hat{n}_{y[0]} \approx \frac{\Omega}{c}\left[\frac{\sin\alpha s}{\left(3\cos^2(\theta_\mathrm{o} - \alpha) + 1\right)^{1/2}} + x_\mathrm{o}\right] + \mathcal{O}\left(\phi^2, (\Omega r_\mathrm{o}/c)^2, \phi\,(\Omega r_\mathrm{o}/c)\right), \tag{17}$$

where we have considered $\Omega r_\mathrm{o}/c \lesssim \phi$, e.g. for a millisecond pulsar with $\Omega \sim 10^2$ Hz and $r_\mathrm{o} \sim 10^6$ cm, such that $\mathcal{O}\left((\Omega r_\mathrm{o}/c)^2\right) \lesssim \mathcal{O}\left(\phi\,(\Omega r_\mathrm{o}/c)\right) \lesssim \mathcal{O}\left(\phi^2\right)$, all to be ignored in our analysis, and have substituted $\phi = \Omega s/c$ in equation (17), the leading order rotational effect to be considered in our analysis.

Now, integrating $\hat{\mathbf{n}}_{[0]} = \mathrm{d}\mathbf{r}/\mathrm{d}s$ with respect to s, the unperturbed (classical) trajectory of the light ray can be derived:

$$x \approx \hat{n}_{x[0]} s + x_{\mathrm{o}}, \tag{18}$$

$$z \approx \hat{n}_{z[0]} s + z_{\mathrm{o}}, \tag{19}$$

$$y \approx \int \hat{n}_{y[0]}\, \mathrm{d}s + y_{\mathrm{o}} = \frac{\Omega}{c} \left[\frac{\sin\alpha s^2}{2\left(3\cos^2(\theta_{\mathrm{o}}-\alpha)+1\right)^{1/2}} + x_{\mathrm{o}} s \right] + y_{\mathrm{o}}, \tag{20}$$

where $\hat{n}_{x[0]}$, $\hat{n}_{z[0]}$, and $\hat{n}_{y[0]}$ are given by equations (15)–(17), respectively, and the emission point is $(x_{\mathrm{o}}, y_{\mathrm{o}}, z_{\mathrm{o}}) = (r_{\mathrm{o}}\sin\theta_{\mathrm{o}}, 0, r_{\mathrm{o}}\cos\theta_{\mathrm{o}})$. Note that the classical trajectory of the light ray approximates to a three-dimensional parabolic curve in the limit $\phi \ll 1$; this results from $\hat{n}_{y[0]}$ growing linearly with s while $\hat{n}_{x[0]}$ and $\hat{n}_{z[0]}$ being constants.[3]

In equation (10) ϑ must be defined as the angle between the classical trajectory of the light ray traced by $\hat{\mathbf{n}}_{[0]}$ and the local magnetic field line $\mathbf{B}$ since $\sin\vartheta$ is considered to be unperturbed in view of equation (10) (see Fig. 1). Then from equations (12) and (13) one can express

$$\cos\vartheta = \hat{\mathbf{n}}_{[0]} \cdot \hat{\mathbf{B}}(r, \theta, \phi) \approx \frac{4\cos(\theta_{\mathrm{o}}-\alpha)\cos(\theta-\alpha) + \sin(\theta_{\mathrm{o}}-\alpha)\sin(\theta-\alpha)}{\left(3\cos^2(\theta_{\mathrm{o}}-\alpha)+1\right)^{1/2}\left(3\cos^2(\theta-\alpha)+1\right)^{1/2}} + \mathcal{O}\left(\phi^2, \phi\,(\Omega r_{\mathrm{o}}/c)\right), \tag{21}$$

taking the leading order expansion in ϕ. In the case of the PM Lagrangian model, one can determine the leading order correction to n by means of equations (10), (12), and (21):

$$\delta n_{[1]} = \eta_2 B^2 \sin^2\vartheta \approx \frac{4\eta_2\mu^2\sin^2(\theta-\theta_{\mathrm{o}})}{\left(3\cos^2(\theta_{\mathrm{o}}-\alpha)+1\right)\rho^6} + \mathcal{O}\left(\phi^2, \phi\,(\Omega r_{\mathrm{o}}/c)\right), \tag{22}$$

where $\rho \equiv \sqrt{x^2+z^2}$ with $x = \rho\sin\theta$ and $z = \rho\cos\theta$. For computational convenience, equation (22) can be rewritten in Cartesian coordinates by substituting $\sin\theta = x/\sqrt{x^2+z^2}$ and $\cos\theta = z/\sqrt{x^2+z^2}$:

$$\delta n_{[1]} \approx \frac{4\eta_2\mu^2(\cos\theta_{\mathrm{o}} x - \sin\theta_{\mathrm{o}} z)^2}{\left(3\cos^2(\theta_{\mathrm{o}}-\alpha)+1\right)\left(x^2+z^2\right)^4}. \tag{23}$$

Using equation (11), one can easily compute the x and z components of $\delta\hat{\mathbf{n}}_{[1]}$:

$$\delta\hat{n}_{x[1]} \approx \int \partial_x \delta n_{[1]}\, \mathrm{d}s = \frac{\delta n_{[1]}}{\hat{n}_{x[0]}}, \tag{24}$$

$$\delta\hat{n}_{z[1]} \approx \int \partial_z \delta n_{[1]}\, \mathrm{d}s = \frac{\delta n_{[1]}}{\hat{n}_{z[0]}}, \tag{25}$$

where $\delta n_{[1]}$ is given by equation (23), and in order to simplify our calculations we have exploited the relation,

$$\mathrm{d}s = \hat{\mathbf{n}}_{[0]} \cdot \mathrm{d}\mathbf{r} = \hat{n}_{x[0]}\mathrm{d}x + \hat{n}_{z[0]}\mathrm{d}z + \hat{n}_{y[0]}\,\mathrm{d}y \approx \hat{n}_{x[0]}\mathrm{d}x + \hat{n}_{z[0]}\mathrm{d}z + \mathcal{O}\left((\Omega r_{\mathrm{o}}/c)^2\right) \approx \frac{\mathrm{d}x}{\hat{n}_{x[0]}} \text{ or } \frac{\mathrm{d}z}{\hat{n}_{z[0]}}, \tag{26}$$

which is due to equations (18)–(20).

To provide further convenience for equation (23), we may re-parametrize the variables x and z given by equations (18) and (19) using a dimensionless parameter $\lambda \geq 0$, defined via $s = r_{\mathrm{o}}\lambda$:

$$x = r_{\mathrm{o}}\left(\hat{n}_{x[0]}\lambda + \sin\theta_{\mathrm{o}}\right), \tag{27}$$

$$z = r_{\mathrm{o}}\left(\hat{n}_{z[0]}\lambda + \cos\theta_{\mathrm{o}}\right), \tag{28}$$

where $\hat{n}_{x[0]}$ and $\hat{n}_{z[0]}$ refer to equations (15) and (16), respectively. It should be noted here that the value of λ is restricted by the condition $\phi \sim \Omega t = \Omega r_{\mathrm{o}}\lambda/c \ll 1$; from this it follows that $\lambda \ll c/(\Omega r_{\mathrm{o}})$. For example for a millisecond pulsar with $\Omega \sim 10^2$ Hz, we shall have $\lambda \ll 10^2$, given $r_{\mathrm{o}} \sim 10^6$ cm.

Inserting equations (27) and (28) into equations (24) and (25) through equation (23), and substituting $s = r_{\mathrm{o}}\lambda$ in equation (17), one can express $\hat{n}_x$, $\hat{n}_z$, and $\hat{n}_y$ in terms of λ:

$$\begin{aligned}\hat{n}_x &= \hat{n}_{x[0]} + \delta\hat{n}_{x[1]} \\ &\approx \hat{n}_{x[0]} + \frac{4\eta_2 B_{\mathrm{o}}^2\sin^2(\theta_{\mathrm{o}}-\alpha)\lambda^2}{\hat{n}_{x[0]}\left(3\cos^2(\theta_{\mathrm{o}}-\alpha)+1\right)\left[\left(3\cos^2(\theta_{\mathrm{o}}-\alpha)+1\right)^{1/2}\lambda^2 + 4\cos(\theta_{\mathrm{o}}-\alpha)\lambda + \left(3\cos^2(\theta_{\mathrm{o}}-\alpha)+1\right)^{1/2}\right]^4},\end{aligned} \tag{29}$$

$$\begin{aligned}\hat{n}_z &= \hat{n}_{z[0]} + \delta\hat{n}_{z[1]} \\ &\approx \hat{n}_{z[0]} + \frac{4\eta_2 B_{\mathrm{o}}^2\sin^2(\theta_{\mathrm{o}}-\alpha)\lambda^2}{\hat{n}_{z[0]}\left(3\cos^2(\theta_{\mathrm{o}}-\alpha)+1\right)\left[\left(3\cos^2(\theta_{\mathrm{o}}-\alpha)+1\right)^{1/2}\lambda^2 + 4\cos(\theta_{\mathrm{o}}-\alpha)\lambda + \left(3\cos^2(\theta_{\mathrm{o}}-\alpha)+1\right)^{1/2}\right]^4},\end{aligned} \tag{30}$$

---

[3] Being projected on to the xz-plane, the curve appears to be a straight line, as represented by the red dashed line in Fig. 1.

$$\hat{n}_y = \hat{n}_{y[0]} \approx \frac{\Omega r_\mathrm{o}}{c}\left[\frac{\sin\alpha\lambda}{\left(3\cos^2(\theta_\mathrm{o}-\alpha)+1\right)^{1/2}} + \sin\theta_\mathrm{o}\right], \tag{31}$$

where $\hat{n}_{x[0]}$ and $\hat{n}_{z[0]}$ refer to equations (15) and (16), respectively, and $B_\mathrm{o} \equiv \mu\left(3\cos^2(\theta_\mathrm{o}-\alpha)+1\right)^{1/2}/r_\mathrm{o}^3$ denotes the magnitude of the magnetic field at the initial point $(x_\mathrm{o}, y_\mathrm{o}, z_\mathrm{o}) = (r_\mathrm{o}\sin\theta_\mathrm{o}, 0, r_\mathrm{o}\cos\theta_\mathrm{o})$. From equations (29)–(31) it is evident that $\hat{\mathbf{n}}$ is no longer a unit vector; $\hat{\mathbf{n}}\cdot\hat{\mathbf{n}} \approx 1 + \mathcal{O}\left(_{[1]}\right) + \mathcal{O}\left((\Omega r_\mathrm{o}/c)^2, _{[2]}\right)$.

Further, by integrating $\hat{\mathbf{n}} = \mathrm{d}\mathbf{r}/\mathrm{d}s = \left(\hat{n}_x, \hat{n}_y, \hat{n}_z\right)$ with respect to s, with $\hat{n}_x$, $\hat{n}_z$, and $\hat{n}_y$ given by equations (29)–(31), one can construct a trajectory curve of the light ray:

$$X \equiv \int_0^s \hat{n}_x\,\mathrm{d}s = r_\mathrm{o}\int_0^\lambda \hat{n}_x\,\mathrm{d}\lambda \approx r_\mathrm{o}\hat{n}_{x[0]}\lambda + \frac{4\eta_2 B_\mathrm{o}^2 r_\mathrm{o}\sin^2(\theta_\mathrm{o}-\alpha)}{\hat{n}_{x[0]}\left(3\cos^2(\theta_\mathrm{o}-\alpha)+1\right)}\mathcal{I}(\lambda), \tag{32}$$

$$Z \equiv \int_0^s \hat{n}_z\,\mathrm{d}s = r_\mathrm{o}\int_0^\lambda \hat{n}_z\,\mathrm{d}\lambda \approx r_\mathrm{o}\hat{n}_{z[0]}\lambda + \frac{4\eta_2 B_\mathrm{o}^2 r_\mathrm{o}\sin^2(\theta_\mathrm{o}-\alpha)}{\hat{n}_{z[0]}\left(3\cos^2(\theta_\mathrm{o}-\alpha)+1\right)}\mathcal{I}(\lambda), \tag{33}$$

$$Y \equiv \int_0^s \hat{n}_y\,\mathrm{d}s = r_\mathrm{o}\int_0^\lambda \hat{n}_{y[0]}\,\mathrm{d}\lambda \approx \frac{\Omega r_\mathrm{o}^2}{c}\left[\frac{\sin\alpha\lambda^2}{2\left(3\cos^2(\theta_\mathrm{o}-\alpha)+1\right)^{1/2}} + \sin\theta_\mathrm{o}\lambda\right], \tag{34}$$

where

$$\begin{aligned}
\mathcal{I}(\lambda) \equiv{}& \int_0^\lambda \frac{\lambda^2}{\left[\left(3\cos^2(\theta_\mathrm{o}-\alpha)+1\right)^{1/2}\lambda^2 + 4\cos(\theta_\mathrm{o}-\alpha)\lambda + \left(3\cos^2(\theta_\mathrm{o}-\alpha)+1\right)^{1/2}\right]^4}\mathrm{d}\lambda \\
={}& \frac{\left(19\cos^2(\theta_\mathrm{o}-\alpha)+1\right)\left(3\cos^2(\theta_\mathrm{o}-\alpha)+1\right)^{1/2}}{16\sin^7(\theta_\mathrm{o}-\alpha)}\arctan\left(\frac{\left(3\cos^2(\theta_\mathrm{o}-\alpha)+1\right)^{1/2}\lambda + 2\cos(\theta_\mathrm{o}-\alpha)}{\sin(\theta_\mathrm{o}-\alpha)}\right) \\
&+\frac{1}{192\sin^6(\theta_\mathrm{o}-\alpha)\left[\left(3\cos^2(\theta_\mathrm{o}-\alpha)+1\right)^{1/2}\lambda^2 + 4\cos(\theta_\mathrm{o}-\alpha)\lambda + \left(3\cos^2(\theta_\mathrm{o}-\alpha)+1\right)^{1/2}\right]^3} \\
&\times\Big[12\left(3\cos^2(\theta_\mathrm{o}-\alpha)+1\right)^{1/2}\left(57\cos^4(\theta_\mathrm{o}-\alpha)+22\cos^2(\theta_\mathrm{o}-\alpha)+1\right)\lambda^5 \\
&+120\cos(\theta_\mathrm{o}-\alpha)\left(57\cos^4(\theta_\mathrm{o}-\alpha)+22\cos^2(\theta_\mathrm{o}-\alpha)+1\right)\lambda^4 \\
&+32\left(3\cos^2(\theta_\mathrm{o}-\alpha)+1\right)^{1/2}\left(266\cos^4(\theta_\mathrm{o}-\alpha)+33\cos^2(\theta_\mathrm{o}-\alpha)+1\right)\lambda^3 \\
&+192\cos(\theta_\mathrm{o}-\alpha)\left(76\cos^4(\theta_\mathrm{o}-\alpha)+23\cos^2(\theta_\mathrm{o}-\alpha)+1\right)\lambda^2 \\
&+12\left(3\cos^2(\theta_\mathrm{o}-\alpha)+1\right)^{1/2}\left(319\cos^4(\theta_\mathrm{o}-\alpha)+82\cos^2(\theta_\mathrm{o}-\alpha)-1\right)\lambda \\
&+8\cos(\theta_\mathrm{o}-\alpha)\left(141\cos^4(\theta_\mathrm{o}-\alpha)+86\cos^2(\theta_\mathrm{o}-\alpha)+13\right)\Big] \\
&-\left\{\mathrm{above}|_{\lambda=0}\right\}.
\end{aligned} \tag{35}$$

For example with $r_\mathrm{o} = 2\times10^6$ cm, $\theta_\mathrm{o} = 60^\circ$, $\alpha = 45^\circ$, $\Omega = 2\pi\times10^2$ Hz, and $\eta_2 B_\mathrm{o}^2 \approx 4.29\times10^{-5}$, we plot a trajectory of our light ray (X/r_o, Y/r_o, Z/r_o) for $0 \le \lambda \le 10$ on a logarithmic scale, as shown in Fig. 2(a). Also, for intuitive visualization, in Fig. 2(b) is plotted the trajectory on a linear scale, with the quantum refraction effect fairly exaggerated by $\eta_2 B_\mathrm{o}^2 \sim 10^4$, which is 10^9 times as large as an actual order $\sim10^{-5}$. Note, in particular, that the trajectory is deflected from a straight line as viewed in the xz-plane (due to the quantum refraction effect), and at the same time that it follows a parabolic path in another plane perpendicular to the xz-plane (due to the rotational effect of the pulsar magnetosphere); therefore, the light ray follows a three-dimensional *twisted* curve. In Appendix A, we provide a detailed discussion of the properties of this curve in reference to the Frenet–Serret formulas (Spivak 1999).

4 CHANGE OF POLARIZATION OF A LIGHT RAY DUE TO QUANTUM REFRACTION

In Section 3, we have separated Cases I and II for the two different values of the refractive index n attributed to the same magnetosphere, depending on the propagation and polarization of the light ray associated with them, as given by equation (9), according to the PM Lagrangian model (Kim & Kim 2022). In accordance with our perturbation analysis, the refractive index can be approximated via expansion as (Adler 1971)

$$n \approx \begin{cases} 1 + \eta_2 B^2\sin^2\vartheta + \mathcal{O}\left(_{[2]}\right) & \text{for Case I,} \\ 1 + \eta_1 B^2\sin^2\vartheta + \mathcal{O}\left(_{[2]}\right) & \text{for Case II,} \end{cases} \tag{36}$$

where $\eta_1 B^2$, $\eta_2 B^2 \lesssim 10^{-4} \ll 1$, and $\mathcal{O}\left(_{[2]}\right)$ is a shorthand expression for $\mathcal{O}\left(\eta_1^2 B^4, \eta_1\eta_2 B^4, \eta_2^2 B^4\right)$. From this, one can see that all the results obtained through the perturbation analysis in Section 3 for Case I can be recycled for Case II simply by replacing η_2 by η_1. That is, the propagation vector and the trajectory curve of our light ray for Case II shall be given by the same expressions as equations (29)–(31) and (32)–(34), respectively, but with η_2 replaced by η_1.

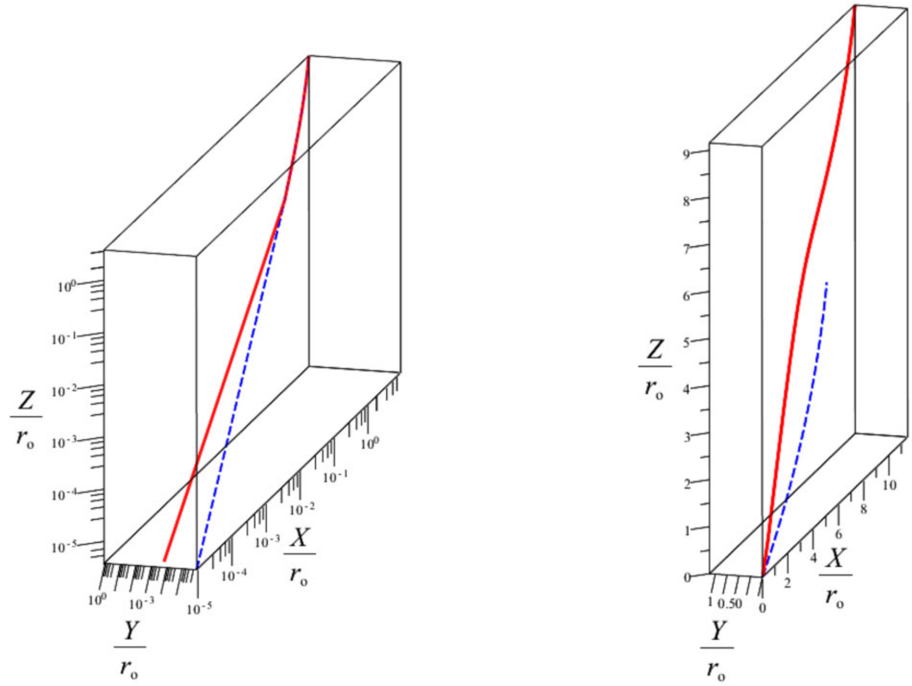

(a) (b)

Figure 2. (a) A trajectory of the light ray ($X/r_{\rm o}$, $Y/r_{\rm o}$, $Z/r_{\rm o}$) plotted against $0 \le \lambda \le 10$ on a logarithmic scale; the red solid curve and the blue dashed curve represent the total trajectory (classical trajectory + quantum correction) and the classical trajectory, respectively. (b) The trajectory plotted on a linear scale for intuitive visualization, with the quantum refraction effect fairly exaggerated by $\eta_2 B_{\rm o}^2 \sim 10^4$, which is 10^9 times as large as an actual order $\sim 10^{-5}$.

In this section, we work out the two polarization vectors of the light ray for Case I and Case II, associated with the dual refractive index given by equation (36); in contrast with the propagation of the ray, there is a distinct difference between them. In relation to this, we discuss quantum birefringence for our pulsar emission at the end.

4.1 For Case I

According to Born et al. (1999), the propagation of the unit polarization vector $\boldsymbol{\varepsilon}$ can be described by the equation:

$$\frac{\mathrm{d}\boldsymbol{\varepsilon}}{\mathrm{d}\tau} \equiv n\frac{\mathrm{d}\boldsymbol{\varepsilon}}{\mathrm{d}s} = -\left(\boldsymbol{\varepsilon}\cdot\nabla\left(\ln n\right)\right)\nabla\mathcal{S}, \tag{37}$$

where $\mathcal{S}(x, y, z) =$ const. represents the geometrical wavefront. Substituting equation (6) into equation (37), we get

$$\frac{\mathrm{d}\boldsymbol{\varepsilon}}{\mathrm{d}s} = -\left(\boldsymbol{\varepsilon}\cdot\nabla\left(\ln n\right)\right)\frac{\mathrm{d}\mathbf{r}}{\mathrm{d}s}. \tag{38}$$

Now, in view of equation (10), we find

$$\ln n \approx \ln\left(1 + \delta n_{[1]} + \mathcal{O}\left(_{[2]}\right)\right) \approx \delta n_{[1]} + \mathcal{O}\left(_{[2]}\right), \tag{39}$$

where $\delta n_{[1]}$ refers to equation (22). Then plugging this into equation (38) and inspecting the orders of both sides, one can derive

$$\frac{\mathrm{d}}{\mathrm{d}s}\left(\delta\boldsymbol{\varepsilon}_{[1]}\right) = -\left[\boldsymbol{\varepsilon}_{[0]}\cdot\nabla\left(\delta n_{[1]}\right)\right]\hat{\mathbf{n}}_{[0]}, \tag{40}$$

where $\boldsymbol{\varepsilon}_{[0]}$ denotes the classical polarization vector, $\delta\boldsymbol{\varepsilon}_{[1]}$ is the leading (first) order quantum correction to it, and $\hat{\mathbf{n}}_{[0]}$ refers to the classical propagation vector. This equation describes how quantum refraction affects the propagation of our polarization vector along the path of the light ray by means of perturbation.

One possible way of prescribing the polarization vector classically, with the consideration of the rotational effect is

$$\boldsymbol{\varepsilon}_{[0]} = \hat{n}_{z[0]}\mathbf{e}_x \pm \hat{n}_{y[0]}\mathbf{e}_y - \hat{n}_{x[0]}\mathbf{e}_z, \tag{41}$$

where $\hat{n}_{x[0]}$, $\hat{n}_{z[0]}$, and $\hat{n}_{y[0]}$ are given by equations (15)–(17), respectively. It can be easily checked out that $\boldsymbol{\varepsilon}_{[0]}$ is orthogonal to the propagation vector, $\hat{\mathbf{n}}_{[0]} = \hat{n}_{x[0]}\mathbf{e}_x + \hat{n}_{y[0]}\mathbf{e}_y + \hat{n}_{z[0]}\mathbf{e}_z$, i.e. $\boldsymbol{\varepsilon}_{[0]}\cdot\hat{\mathbf{n}}_{[0]} \approx 0 + \mathcal{O}\left((\Omega r_{\rm o}/c)^2\right)$ while it is normalized, i.e. $\boldsymbol{\varepsilon}_{[0]}^2 \approx 1 + \mathcal{O}\left((\Omega r_{\rm o}/c)^2\right)$.

Following Kim & Kim (2022), the initial polarization vector associated with n for Case I in accordance with equation (9) can be expressed as

$$\boldsymbol{\varepsilon}_{\rm o} = \left(1 - \eta_1 B_{\rm o}^2 + 2\eta_2 B_{\rm o}^2\right)\hat{n}_{z[0]}\mathbf{e}_x \pm \hat{n}_{y[0]}\big|_{s=0}\mathbf{e}_y - \left(1 - \eta_1 B_{\rm o}^2\right)\hat{n}_{x[0]}\mathbf{e}_z, \tag{42}$$

which has been adapted from its original expression in Kim & Kim (2022) to the geometry of our rotating magnetosphere, with the consideration of equation (41).[4] Then, we may separate the classical part,

$$\boldsymbol{\varepsilon}_{\mathrm{o}[0]} \equiv \boldsymbol{\varepsilon}_{[0]}\big|_{s=0} = \hat{n}_{z[0]}\mathbf{e}_x \pm \hat{n}_{y[0]}\big|_{s=0}\mathbf{e}_y - \hat{n}_{x[0]}\mathbf{e}_z \tag{43}$$

and the quantum correction,

$$\delta\boldsymbol{\varepsilon}_{\mathrm{o}[1]} = \left(-\eta_1 B_{\mathrm{o}}^2 + 2\eta_2 B_{\mathrm{o}}^2\right)\hat{n}_{z[0]}\mathbf{e}_x + \eta_1 B_{\mathrm{o}}^2 \hat{n}_{x[0]}\mathbf{e}_z. \tag{44}$$

The polarization vector with the first-order correction due to the quantum refraction effect can be obtained in a similar manner as in Section 3. Integrating equation (40) with respect to $s = r_{\mathrm{o}}\lambda$, and combining this with equation (41), and using equations (23), (26), (27), (28), (41), and (44), we finally have $\boldsymbol{\varepsilon} = \varepsilon_x\mathbf{e}_x + \varepsilon_y\mathbf{e}_y + \varepsilon_z\mathbf{e}_z$ with

$$\begin{aligned}\varepsilon_x &= \varepsilon_{x[0]} + \delta\varepsilon_{x[1]} \\ &\approx \hat{n}_{z[0]} + \left(-\eta_1 B_{\mathrm{o}}^2 + 2\eta_2 B_{\mathrm{o}}^2\right)\hat{n}_{z[0]} \\ &\quad - \frac{4\eta_2 B_{\mathrm{o}}^2 \sin^2(\theta_{\mathrm{o}} - \alpha)\left(\hat{n}_{z[0]}^2 - \hat{n}_{x[0]}^2\right)\lambda^2}{\hat{n}_{z[0]}\left(3\cos^2(\theta_{\mathrm{o}} - \alpha) + 1\right)\left[\left(3\cos^2(\theta_{\mathrm{o}} - \alpha) + 1\right)^{1/2}\lambda^2 + 4\cos(\theta_{\mathrm{o}} - \alpha)\lambda + \left(3\cos^2(\theta_{\mathrm{o}} - \alpha) + 1\right)^{1/2}\right]^4},\end{aligned} \tag{45}$$

$$\begin{aligned}\varepsilon_z &= \varepsilon_{z[0]} + \delta\varepsilon_{z[1]} \\ &\approx -\hat{n}_{x[0]} + \eta_1 B_{\mathrm{o}}^2 \hat{n}_{x[0]} \\ &\quad - \frac{4\eta_2 B_{\mathrm{o}}^2 \sin^2(\theta_{\mathrm{o}} - \alpha)\left(\hat{n}_{z[0]}^2 - \hat{n}_{x[0]}^2\right)\lambda^2}{\hat{n}_{x[0]}\left(3\cos^2(\theta_{\mathrm{o}} - \alpha) + 1\right)\left[\left(3\cos^2(\theta_{\mathrm{o}} - \alpha) + 1\right)^{1/2}\lambda^2 + 4\cos(\theta_{\mathrm{o}} - \alpha)\lambda + \left(3\cos^2(\theta_{\mathrm{o}} - \alpha) + 1\right)^{1/2}\right]^4},\end{aligned} \tag{46}$$

$$\begin{aligned}\varepsilon_y &= \varepsilon_{y[0]} + \delta\varepsilon_{y[1]} \\ &\approx \pm\hat{n}_{y[0]} - \frac{4\eta_2 B_{\mathrm{o}}^2 \sin^2(\theta_{\mathrm{o}} - \alpha)\left(\hat{n}_{z[0]}^2 - \hat{n}_{x[0]}^2\right)}{\hat{n}_{x[0]}\hat{n}_{z[0]}\left(3\cos^2(\theta_{\mathrm{o}} - \alpha) + 1\right)}\left[\frac{\hat{n}_{y[0]}\lambda^2}{\left[\left(3\cos^2(\theta_{\mathrm{o}} - \alpha) + 1\right)^{1/2}\lambda^2 + 4\cos(\theta_{\mathrm{o}} - \alpha)\lambda + \left(3\cos^2(\theta_{\mathrm{o}} - \alpha) + 1\right)^{1/2}\right]^4}\right. \\ &\quad \left. - \frac{\Omega r_{\mathrm{o}}\sin\alpha}{c\left(3\cos^2(\theta_{\mathrm{o}} - \alpha) + 1\right)^{1/2}}\mathcal{I}(\lambda)\right],\end{aligned} \tag{47}$$

where $\hat{n}_{x[0]}$, $\hat{n}_{z[0]}$, and $\hat{n}_{y[0]}$ are given by equations (15), (16), and (31), respectively, and $B_{\mathrm{o}} = \mu\left(3\cos^2(\theta_{\mathrm{o}} - \alpha) + 1\right)^{1/2}/r_{\mathrm{o}}^3$ and $\mathcal{I}(\lambda)$ refers to equation (35). In Fig. 3 is plotted the change in the polarization vector $\left(\Delta\varepsilon_x, \Delta\varepsilon_y, \Delta\varepsilon_z\right) \equiv \left(\varepsilon_x(\lambda), \varepsilon_y(\lambda), \varepsilon_z(\lambda)\right)\big|_0^\lambda$ against $0 \leq \lambda \leq 10$ on a logarithmic scale, wherein $r_{\mathrm{o}} = 2 \times 10^6$ cm, $\theta_{\mathrm{o}} = 60^\circ$, $\alpha = 45^\circ$, $\Omega = 2\pi \times 10^2$ Hz, $\eta_1 B_{\mathrm{o}}^2 \approx 2.45 \times 10^{-5}$, and $\eta_2 B_{\mathrm{o}}^2 \approx 4.29 \times 10^{-5}$. From this plot, one can see that the total polarization vector changes drastically along the *x*-axis and *z*-axis near the beginning of the propagation of our light ray due to the quantum refraction effect, while the classical polarization vector changes only along the *y*-axis due to the rotational effect, as can be seen from equation (41).

By equations (29)–(31) and (45)–(47) one can inspect the orthogonality between the propagation and polarization vectors, $\hat{\mathbf{n}}$ and $\boldsymbol{\varepsilon}$:

$$\hat{\mathbf{n}} \cdot \boldsymbol{\varepsilon} \approx 2\eta_2 B_{\mathrm{o}}^2 \hat{n}_{x[0]}\hat{n}_{z[0]} + \mathcal{O}\left((\Omega r_{\mathrm{o}}/c)^2, {}_{[2]}\right), \tag{48}$$

where $\hat{n}_{x[0]}$ and $\hat{n}_{z[0]}$ are given by equations (15) and (16), respectively. This implies that the quantum refraction effect results in breaking the orthogonality at the leading order in $\eta_2 B_{\mathrm{o}}^2$. However, the departure from the orthogonality remains constant under this effect, being determined at the leading order in $\eta_2 B_{\mathrm{o}}^2$ solely by the initial conditions for quantum refraction. For example with $r_{\mathrm{o}} = 2 \times 10^6$ cm, $\theta_{\mathrm{o}} = 60^\circ$, $\alpha = 45^\circ$, and a usual value of $\eta_2 B_{\mathrm{o}}^2 \approx 4.29 \times 10^{-5}$, we find the departure value to be $\sin^{-1}(\hat{\mathbf{n}} \cdot \boldsymbol{\varepsilon}) \approx 3.02 \times 10^{-5}$ rad.

Using equations (41) and (45)–(47), the Faraday rotation angle can be determined via

$$\varphi_{\mathrm{F}} \equiv \cos^{-1}\left(\boldsymbol{\varepsilon}_{[0]} \cdot \hat{\boldsymbol{\varepsilon}}\right) \approx \sqrt{\delta\boldsymbol{\varepsilon}_{[1]}^2 - \left(\boldsymbol{\varepsilon}_{[0]} \cdot \delta\boldsymbol{\varepsilon}_{[1]}\right)^2} + \mathcal{O}\left((\Omega r_{\mathrm{o}}/c)^2, {}_{[2]}\right). \tag{49}$$

For example with $r_{\mathrm{o}} = 2 \times 10^6$ cm, $\theta_{\mathrm{o}} = 60^\circ$, $\alpha = 45^\circ$, and usual values of $\eta_1 B_{\mathrm{o}}^2 \approx 2.45 \times 10^{-5}$, $\eta_2 B_{\mathrm{o}}^2 \approx 4.29 \times 10^{-5}$, we find $\varphi_{\mathrm{F}} \approx 3.02 \times 10^{-5}$ rad.

Note that the values, $\sin^{-1}(\hat{\mathbf{n}} \cdot \boldsymbol{\varepsilon}) \approx 3.02 \times 10^{-5}$ rad and $\varphi_{\mathrm{F}} \approx 3.02 \times 10^{-5}$ rad, obtained as above are small but comparable to our perturbation parameters, $\eta_1 B_{\mathrm{o}}^2 \approx 2.45 \times 10^{-5}$ and $\eta_2 B_{\mathrm{o}}^2 \approx 4.29 \times 10^{-5}$; therefore, these effects are truly quantum refractive.

---

[4] Originally, in Kim & Kim (2022) the initial polarization vector associated with n for Case I is given by $\boldsymbol{\varepsilon}_{\mathrm{o}} = \left(1 - \eta_1 B_{\mathrm{o}}^2 + 2\eta_2 B_{\mathrm{o}}^2\right)\cos\theta\,\mathbf{e}_x - \left(1 - \eta_1 B_{\mathrm{o}}^2\right)\sin\theta\,\mathbf{e}_z$, which corresponds to the classical polarization vector, $\boldsymbol{\varepsilon}_{[0]} = \cos\theta\,\mathbf{e}_x - \sin\theta\,\mathbf{e}_z$.

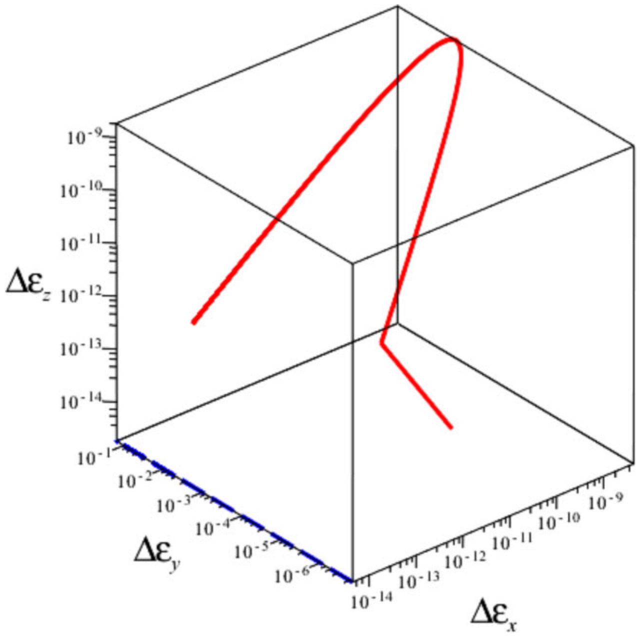

Figure 3. The change in the polarization vector, $\left(\Delta\varepsilon_x, \Delta\varepsilon_y, \Delta\varepsilon_z\right) \equiv \left(\varepsilon_x(\lambda), \varepsilon_y(\lambda), \varepsilon_z(\lambda)\right)\big|_0^\lambda$ plotted against $0 \le \lambda \le 10$ on a logarithmic scale; the red solid curve and the blue dashed curve represent the total polarization vector (classical polarization vector + quantum correction) and the classical polarization vector, respectively.

4.2 For Case II

One can write down the classical polarization vector associated with the refractive index n for Case II as given by (9), with the consideration of the rotational effect as

$$\boldsymbol{\varepsilon}_{[0]} = -\left(\hat{n}_{x[0]} + \hat{n}_{z[0]}\right)\hat{n}_{y[0]}\mathbf{e}_x + \mathbf{e}_y + \left(\hat{n}_{x[0]} - \hat{n}_{z[0]}\right)\hat{n}_{y[0]}\mathbf{e}_z, \tag{50}$$

where $\hat{n}_{x[0]}$, $\hat{n}_{z[0]}$, and $\hat{n}_{y[0]}$ are given by equations (15)–(17), respectively. In accordance with this, the initial polarization vector shall be

$$\boldsymbol{\varepsilon}_{\rm o} = -\left(\hat{n}_{x[0]} + \hat{n}_{z[0]}\right)\hat{n}_{y[0]}\big|_{s=0}\mathbf{e}_x + \mathbf{e}_y + \left(\hat{n}_{x[0]} - \hat{n}_{z[0]}\right)\hat{n}_{y[0]}\big|_{s=0}\mathbf{e}_z, \tag{51}$$

which has been adapted from its original expression in Kim & Kim (2022) to the geometry of our rotating magnetosphere.[5]

It can be checked out that $\boldsymbol{\varepsilon}_{[0]}$ is orthogonal to the propagation vector, $\hat{\mathbf{n}}_{[0]} = \hat{n}_{x[0]}\mathbf{e}_x + \hat{n}_{y[0]}\mathbf{e}_y + \hat{n}_{z[0]}\mathbf{e}_z$, i.e. $\boldsymbol{\varepsilon}_{[0]} \cdot \hat{\mathbf{n}}_{[0]} = 0$ while it is normalized, i.e. $\boldsymbol{\varepsilon}_{[0]}^2 \approx 1 + \mathcal{O}\left((\Omega r_{\rm o}/c)^2\right)$. In addition, from equations (41) and (50) we find that $\boldsymbol{\varepsilon}_{[0]\,(\text{Case I})} \cdot \boldsymbol{\varepsilon}_{[0]\,(\text{Case II})} = 0$. Then one can note that the three vectors, $\hat{\mathbf{n}}_{[0]}$, $\boldsymbol{\varepsilon}_{[0]\,(\text{Case I})}$, and $\boldsymbol{\varepsilon}_{[0]\,(\text{Case II})}$ form a classical orthonormal basis.[6]

The polarization vector with the first-order correction due to the quantum refraction effect can be obtained in the same manner as in Case I above. That is, we combine the classical polarization vector $\boldsymbol{\varepsilon}_{[0]}$ (given by equation 50) and the quantum correction (given by the integral of equation 40 with respect to $s = r_{\rm o}\lambda$, wherein the refractive index is expressed with η_1, following equation 36). We obtain $\boldsymbol{\varepsilon} = \varepsilon_x\mathbf{e}_x + \varepsilon_y\mathbf{e}_y + \varepsilon_z\mathbf{e}_z$ with

$$\begin{aligned}\varepsilon_x &= \varepsilon_{x[0]} + \delta\varepsilon_{x[1]}\\ &\approx -\left(\hat{n}_{x[0]} + \hat{n}_{z[0]}\right)\hat{n}_{y[0]} + \frac{8\eta_1 B_{\rm o}^2 \sin^2(\theta_{\rm o} - \alpha)}{3\cos^2(\theta_{\rm o} - \alpha) + 1}\left[\frac{\left(\hat{n}_{x[0]} + \hat{n}_{z[0]}\right)\hat{n}_{y[0]}\lambda^2}{\left[\left(3\cos^2(\theta_{\rm o} - \alpha) + 1\right)^{1/2}\lambda^2 + 4\cos(\theta_{\rm o} - \alpha)\lambda + \left(3\cos^2(\theta_{\rm o} - \alpha) + 1\right)^{1/2}\right]^4}\right.\\ &\qquad\left. - \frac{\Omega r_{\rm o}\left(\hat{n}_{x[0]} + \hat{n}_{z[0]}\right)\sin\alpha}{c\left(3\cos^2(\theta_{\rm o} - \alpha) + 1\right)^{1/2}}\mathcal{I}(\lambda)\right],\end{aligned} \tag{52}$$

---

[5] In Kim & Kim (2022) the initial polarization vector associated with n for Case II is given by $\boldsymbol{\varepsilon}_{\rm o} = \mathbf{e}_y$, which is identical to the classical polarization vector, $\boldsymbol{\varepsilon}_{[0]} = \mathbf{e}_y$.

[6] From Appendix A one can see that $\hat{\mathbf{n}}_{[0]} = \mathbf{T}_{[0]} = \hat{n}_{x[0]}\mathbf{e}_x + \hat{n}_{y[0]}\mathbf{e}_y + \hat{n}_{z[0]}\mathbf{e}_z$, $\boldsymbol{\varepsilon}_{[0]\,(\text{Case I})} = \mathbf{N}_{[0]} = \hat{n}_{z[0]}\mathbf{e}_x + \hat{n}_{y[0]}\mathbf{e}_y - \hat{n}_{x[0]}\mathbf{e}_z$, and $\boldsymbol{\varepsilon}_{[0]\,(\text{Case II})} = \mathbf{B}_{[0]} = -\left(\hat{n}_{x[0]} + \hat{n}_{z[0]}\right)\hat{n}_{y[0]}\mathbf{e}_x + \mathbf{e}_y + \left(\hat{n}_{x[0]} - \hat{n}_{z[0]}\right)\hat{n}_{y[0]}\mathbf{e}_z$, where $\mathbf{T}_{[0]}$, $\mathbf{N}_{[0]}$, and $\mathbf{B}_{[0]}$ denote the unperturbed (classical) part of the unit tangent, normal, and bi-normal vectors, taken from equations (A2)–(A4), respectively, with all the terms of $\delta n_{[1]}$ removed.

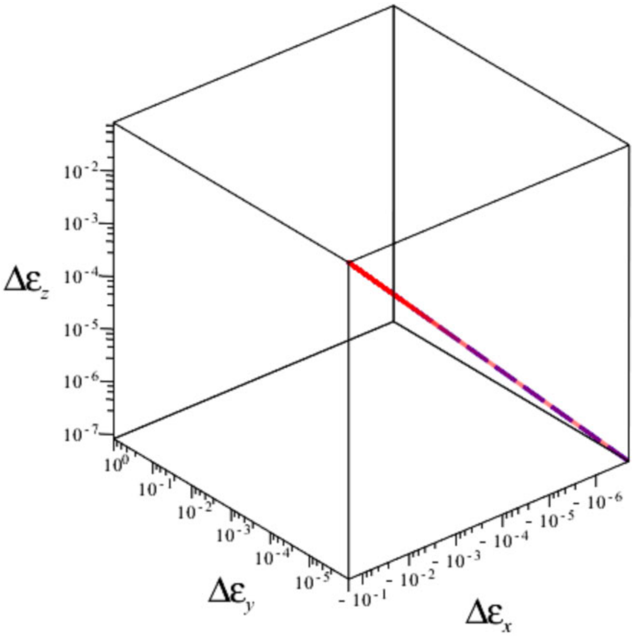

Figure 4. The change in the polarization vector, $\left(\Delta\varepsilon_x, \Delta\varepsilon_y, \Delta\varepsilon_z\right) \equiv \left(\varepsilon_x(\lambda), \varepsilon_y(\lambda), \varepsilon_z(\lambda)\right)\big|_0^{\lambda}$ plotted against $0 \leq \lambda \leq 10$ on a logarithmic scale; the red solid curve and the blue dashed curve represent the total polarization vector (classical polarization vector + quantum correction) and the classical polarization vector, respectively.

$$\begin{aligned}\varepsilon_z &= \varepsilon_{z[0]} + \delta\varepsilon_{z[1]}\\ &\approx \left(\hat{n}_{x[0]} - \hat{n}_{z[0]}\right)\hat{n}_{y[0]} + \frac{8\eta_1 B_{\mathrm{o}}^2 \sin^2\left(\theta_{\mathrm{o}} - \alpha\right)}{3\cos^2\left(\theta_{\mathrm{o}} - \alpha\right) + 1}\left[\frac{-\left(\hat{n}_{x[0]} - \hat{n}_{z[0]}\right)\hat{n}_{y[0]}\lambda^2}{\left[\left(3\cos^2\left(\theta_{\mathrm{o}} - \alpha\right) + 1\right)^{1/2}\lambda^2 + 4\cos\left(\theta_{\mathrm{o}} - \alpha\right)\lambda + \left(3\cos^2\left(\theta_{\mathrm{o}} - \alpha\right) + 1\right)^{1/2}\right]^4}\right.\\ &\quad\left. + \frac{\Omega r_{\mathrm{o}}\left(\hat{n}_{x[0]} - \hat{n}_{z[0]}\right)\sin\alpha}{c\left(3\cos^2\left(\theta_{\mathrm{o}} - \alpha\right) + 1\right)^{1/2}}\mathcal{I}(\lambda)\right], \end{aligned} \tag{53}$$

$$\varepsilon_y = \varepsilon_{y[0]} + \delta\varepsilon_{y[1]} \approx 1 + \mathcal{O}\left(\left(\Omega r_{\mathrm{o}}/c\right)^2\right), \tag{54}$$

where $\hat{n}_{x[0]}$, $\hat{n}_{z[0]}$, and $\hat{n}_{y[0]}$ are given by equations (15), (16), and (31), respectively, and $B_{\mathrm{o}} = \mu\left(3\cos^2\left(\theta_{\mathrm{o}} - \alpha\right) + 1\right)^{1/2}/r_{\mathrm{o}}^3$, and $\mathcal{I}(\lambda)$ refers to equation (35). In Fig. 4 is plotted the change in the polarization vector $\left(\Delta\varepsilon_x, \Delta\varepsilon_y, \Delta\varepsilon_z\right) \equiv \left(\varepsilon_x(\lambda), \varepsilon_y(\lambda), \varepsilon_z(\lambda)\right)\big|_0^{\lambda}$ against $0 \leq \lambda \leq 10$ on a logarithmic scale, wherein $r_{\mathrm{o}} = 2 \times 10^6$ cm, $\theta_{\mathrm{o}} = 60^\circ$, $\alpha = 45^\circ$, $\Omega = 2\pi \times 10^2$ Hz, and $\eta_1 B_{\mathrm{o}}^2 \approx 2.45 \times 10^{-5}$. From this plot, one can see virtually no difference between the total polarization vector and the classical polarization vector; practically, no quantum refraction effect exists. However, the polarization vector changes along the x-axis and z-axis due to the rotational effect, as can be seen from equation (50).

The orthogonality between the propagation and polarization vectors, $\hat{\mathbf{n}}$ and $\boldsymbol{\varepsilon}$ can be inspected using equations (29)–(31) and (52)–(54):

$$\begin{aligned}\hat{\mathbf{n}} \cdot \boldsymbol{\varepsilon} \approx{}& \frac{4\eta_1 B_{\mathrm{o}}^2 \sin^2\left(\theta_{\mathrm{o}} - \alpha\right)\left(\hat{n}_{x[0]}^2 - \hat{n}_{z[0]}^2\right)\hat{n}_{y[0]}\lambda^2}{\hat{n}_{x[0]}\hat{n}_{z[0]}\left(3\cos^2\left(\theta_{\mathrm{o}} - \alpha\right) + 1\right)\left[\left(3\cos^2\left(\theta_{\mathrm{o}} - \alpha\right) + 1\right)^{1/2}\lambda^2 + 4\cos\left(\theta_{\mathrm{o}} - \alpha\right)\lambda + \left(3\cos^2\left(\theta_{\mathrm{o}} - \alpha\right) + 1\right)^{1/2}\right]^4}\\ &- \frac{8\eta_1 B_{\mathrm{o}}^2 \Omega r_{\mathrm{o}} \sin\alpha \sin^2\left(\theta_{\mathrm{o}} - \alpha\right)}{c\left(3\cos^2\left(\theta_{\mathrm{o}} - \alpha\right) + 1\right)^{3/2}}\mathcal{I}(\lambda) + \mathcal{O}\left(\left(\Omega r_{\mathrm{o}}/c\right)^2, {}_{[2]}\right), \end{aligned} \tag{55}$$

where $\hat{n}_{x[0]}$, $\hat{n}_{z[0]}$, and $\hat{n}_{y[0]}$ are given by equations (15), (16), and (31), respectively, and $\mathcal{I}(\lambda)$ refers to equation (35). This implies that the quantum refraction effect results in breaking the orthogonality at the leading order in $\eta_1 B_{\mathrm{o}}^2$. Note here that unlike Case I the departure from the orthogonality changes over the propagation of the light ray under this effect. For example with $r_{\mathrm{o}} = 2 \times 10^6$ cm, $\theta_{\mathrm{o}} = 60^\circ$, $\alpha = 45^\circ$, $\Omega = 2\pi \times 10^2$ Hz, and a usual value of $\eta_1 B_{\mathrm{o}}^2 \approx 2.45 \times 10^{-5}$, we find the maximum departure value to be $\sin^{-1}\left(\hat{\mathbf{n}} \cdot \boldsymbol{\varepsilon}\right) \approx 1.05 \times 10^{-10}$ rad.

Using equations (50) and (52)–(54), the Faraday rotation angle can be determined via

$$\varphi_{\mathrm{F}} = \cos^{-1}\left(\boldsymbol{\varepsilon}_{[0]} \cdot \hat{\boldsymbol{\varepsilon}}\right) \approx \sqrt{\delta\boldsymbol{\varepsilon}_{[1]}^2 - \left(\boldsymbol{\varepsilon}_{[0]} \cdot \delta\boldsymbol{\varepsilon}_{[1]}\right)^2} + \mathcal{O}\left(\left(\Omega r_{\mathrm{o}}/c\right)^2, {}_{[2]}\right). \tag{56}$$

For example with $r_{\mathrm{o}} = 2 \times 10^6$ cm, $\theta_{\mathrm{o}} = 60^\circ$, $\alpha = 45^\circ$, $\Omega = 2\pi \times 10^2$ Hz, and a usual value of $\eta_1 B_{\mathrm{o}}^2 \approx 2.45 \times 10^{-5}$, we find $\varphi_{\mathrm{F}} \approx 1.74 \times 10^{-10}$ rad.

Note that the values, $\sin^{-1}(\hat{\mathbf{n}}\cdot\boldsymbol{\varepsilon}) \approx 1.05\times 10^{-10}$ rad and $\varphi_{\rm F} \approx 1.74\times 10^{-10}$ rad, obtained as above are extremely small compared to our perturbation parameter $\eta_1 B_{\rm o}^2 \approx 2.45\times 10^{-5}$; therefore, these quantum refraction effects can be considered practically negligible.

4.3 Quantum birefringence

From equations (48) and (55) above, one can note the following: the polarization vector partly has a longitudinal component (i.e. a component parallel to the propagation vector) for Case I, whereas it is substantially perpendicular to the propagation vector for Case II. This is because given the conditions for pulsar emission as above, we have $\sin^{-1}\left(\hat{\mathbf{n}}\cdot\boldsymbol{\varepsilon}_{(\rm Case\ I)}\right) \approx 3.02\times 10^{-5}$ rad, which is small but comparable to the perturbation parameter $\eta_2 B_{\rm o}^2 \approx 4.29\times 10^{-5}$, and therefore not negligible, while $\sin^{-1}\left(\hat{\mathbf{n}}\cdot\boldsymbol{\varepsilon}_{(\rm Case\ II)}\right) \approx 1.05\times 10^{-10}$ rad is practically negligible compared to the perturbation parameter $\eta_1 B_{\rm o}^2 \approx 2.45\times 10^{-5}$. The two different polarization modes, together with the dual refractive index n as given by equation (36), are entirely due to the quantum refraction effect. These optical properties can be considered to define 'quantum birefringence' as the phenomenology involved is analogous to classical birefringence.

Classically, birefringence is a well-known phenomenon in crystal optics, but the quantum birefringence considered here has a notable difference from the crystal birefringence. The modes in crystal birefringence are determined by solving the characteristic equation $\Lambda_{ij}\varepsilon_j = 0$, where ε_i represents the mode polarization vector and the matrix Λ_{ij} is given by

$$\Lambda_{ij} = \begin{pmatrix} n_1^2 - n^2\cos^2\theta & 0 & n^2\cos\theta\sin\theta \\ 0 & n_2^2 - n^2 & 0 \\ n^2\cos\theta\sin\theta & 0 & n_3^2 - n^2\sin^2\theta \end{pmatrix}, \tag{57}$$

with n being the refractive index of the medium for the propagation of the probe light and n_i being the principal refractive indices of the crystal (Fowles 1975). It is assumed that the coordinate axes are aligned with the principal axes of the crystal, and the probe light's propagation direction is $(\sin\theta, 0, \cos\theta)$. Note that the principal indices are determined solely by the material properties, irrespective of the probe light's propagation direction.

In fact, one can reproduce the characteristic matrix for the PM Lagrangian with a uniform magnetic field (Kim & Kim 2022) by making the following substitution in equation (57):

$$n_1^2 = 1, \quad n_2^2 = \frac{1-\eta_1 B^2}{1-\eta_1 B^2(1+2\sin^2\theta)}, \quad n_3^2 = \frac{1+(2\eta_2-\eta_1)B^2}{1-\eta_1 B^2}, \tag{58}$$

where the magnetic field is directed along the z-axis. Now, the second *effective* principal index, n_2 depends on the probe light's propagation direction, which is a notable difference from the case of crystal birefringence. This implies that the response of virtual electron–positron pairs in the vacuum can be more involved than that of bound electrons in crystals. As the PM Lagrangian is the generic form of non-linear Lagrangian in the weak field limit, such complication can be regarded as a generic feature of the field-modified vacuum.

5 CONCLUSIONS AND DISCUSSION

We have investigated the quantum refraction effects on the propagation and polarization of a photon in the dipole magnetic field background in pulsar emission, based on the PM Lagrangian from the HES one-loop action. Our main results are given by equations (29)–(31) and (32)–(34) (for the effects on the propagation) and by equations (45)–(47) and (52)–(54) (for the effects on the polarization); via perturbation analysis, we have determined the leading-order corrections to both the propagation and polarization vectors due to quantum refraction, which result in the deflection of the propagation (as shown by Fig. 2) and the change of the two polarization modes (as shown by Figs 3 and 4). Further, we have inspected how quantum refraction affects the orthogonality between the propagation and polarization vectors and the Faraday rotation angle, the results of which are given in the texts at the end of Sections 4.1 and 4.2 for the two polarization modes. From the dual refractive index and the associated polarization modes under the effect of quantum refraction, we have discussed quantum birefringence, with the optical phenomenology analogous to classical birefringence.

It is interesting to compare our analysis with other similar studies on the same topic. For instance, among others, Heyl & Shaviv (2000) have set-up the evolution equation $\partial\mathbf{s}/\partial r = \hat{\Omega}\times\mathbf{s}$ for the 'Stokes vector' $\mathbf{s}$, where the 'birefringent vector' $\hat{\Omega}$ contains the information about the propagation of a photon (e.g. from pulsar radiation) through an inhomogeneous birefringent medium (e.g. a strongly magnetized vacuum in the pulsar magnetosphere). Solving this equation, they have determined the vacuum QED effect from the strong magnetic field on the decoupling of the polarization modes in pulsar emission. Their analysis can be applied to a pulsar environment wherein emission of radiation can take place at various energy scales; the QED effect may enable observations to distinguish between different mechanisms of pulsar emission and to reconstruct the structure of the magnetosphere. In contrast, we have shown the QED effect on the photon polarization in a different way, by solving equation (40) for the transport of the polarization vector along the photon propagation. Despite the difference between the two approaches, the QED effects on the photon polarization might be amenable to the same interpretation, that is, the Faraday rotation (Caiazzo 2019). It will be of great interest to extend our study to a more general situation, where we cover various wavebands of radiation from an oblique rotator and investigate the frequency-dependent effect on the polarization modes. This is considered for our follow-up studies.

It should be noted that not only the quantum refraction due to strong fields but also the plasmas spreading around the magnetosphere might affect the propagation and polarization of radiation. In a broad spectrum of curvature radiation, the low frequency part, e.g. radio emission, is dominated by the plasma effects, while the high frequency part, e.g. X-ray emission, is dominated by the quantum refraction effects, as is well discussed in Wang & Lai (2007). To take the plasma effects into account properly, a good plasma distribution model is required, which is hardly available except for specific computational simulations (Petri 2016). In contrast, our analysis for the quantum refraction effects is well-defined given a specific configuration of coherent magnetic fields (Kim & Trippe 2021). Therefore, for observation of quantum refraction effects, X-ray emission is more favoured than other emissions in the lower frequency regime; e.g. a space telescope (the *Imaging X-ray Polarimetry Explorer*) performed the X-ray polarimetry ($\sim$ a few keV) to confirm the quantum refraction effects for a magnetar (Taverna et al. 2022).

In this analysis, we have not considered the effects of gravitation around the neutron star. As implied by Fig. 1, the magnetic field geometry would be affected by gravitation due to the neutron star mass; the closer to the neutron star surface, the stronger the gravitational effect is, which results in the field lines being more curved inwards. Consequently, the curvature radiation produced along the field lines would also be affected; its pulse profiles would change as the intensity of the radiation field would increase due to the effect of gravitation (Kim & Trippe 2021). In addition, the trajectories of photons would be affected by gravitation too; they should follow the ‘geodesics’ of a curved space–time geometry. For example Heyl et al. (2003) and Caiazzo (2019) have taken this into consideration in studying the evolution of the photon polarization under the vacuum QED effect in pulsar emissions. Inclusion of these gravitational effects is also considered for our follow-up studies.

ACKNOWLEDGEMENTS

D-HK was supported by the Basic Science Research Program through the National Research Foundation of Korea (NRF) funded by the Ministry of Education (NRF-2021R1I1A1A01054781). CMK and SPK were supported by Institute for Basic Science (IBS) under IBS-R012-D1. CMK was also supported by Ultrashort Quantum Beam Facility operation programe (140011) through APRI, GIST, and GIST Research Institute (GRI) grant funded by GIST. SPK was also in part supported by National Research Foundation of Korea (NRF) funded by the Ministry of Education (NRF-2019R1I1A3A01063183).

DATA AVAILABILITY

REFERENCES

Adler S. L., 1971, Ann. Phys., 67, 599
Blandford R. D., Payne D. G., 1982, MNRAS, 199, 883
Born M. et al., 1999, Principles of Optics: Electromagnetic Theory of Propagation, Interference and Diffraction of Light, 7th edn. Cambridge Univ. Press, Cambridge
Caiazzo I., 2019, PhD thesis, Univ. British Columbia, https://open.library.ubc.ca/collections/ubctheses/24/items/1.0387445http://dx.doi.org/10.14288/1.0387445
Caiazzo I., Heyl J., 2018, Phys. Rev. D, 97, 083001
Caiazzo I., Heyl J., 2021, MNRAS, 501, 109
Caiazzo I., González-Caniulef D., Heyl J., Fernández R., 2022, MNRAS, 514, 5024
Ejlli A., Della Valle F., Gastaldi U., Messineo G., Pengo R., Ruoso G., Zavattini G., 2020, Phys. Rept., 871, 1
Euler H., Kockel B., 1935, Die Naturwissenschaften, 23, 246
Fedotov A., Ilderton A., Karbstein F., King B., Seipt D., Taya H., Torgrimsson G., 2023, Phys. Rept., 1010, 1
Fowles G. R., 1975, Introduction to Modern Optics, 2nd edn. Holt, Rinehart and Winston, Inc., New York
Gangadhara R. T., 2005, ApJ, 628, 923
Hattori K., Itakura K., Ozaki S., 2023, Prog. Part. Nucl. Phys., 133, 104068
Heisenberg W., Euler H., 1936, Zeitschr. Phys, 98, 714
Heyl J., Caiazzo I., 2018, Galaxies, 6, 76
Heyl J. S., Shaviv N. J., 2000, MNRAS, 311, 555
Heyl J. S., Shaviv N. J., 2002, Phys. Rev. D, 66, 023002
Heyl J. S., Shaviv N. J., Lloyd D., 2003, MNRAS, 342, 134
Kaspi V. M., Beloborodov A. M., 2017, ARA&A, 55, 261
Kim C. M., Kim S. P., 2022, 3 + 1 Formulation of Light Modes in Nonlinear Electrodynamics: Minkowski Spacetime, preprint (arXiv:2210.12890)
Kim C. M., Kim S. P., 2023, Eur. Phys. J. C, 83, 104
Kim D.-H., Trippe S., 2021, General Relativistic Effects on Pulsar Radiation. preprint (arXiv:2109.13387)
Kong L.-D. et al., 2022, ApJ, 933, L3
Ni W.-T., Mei H.-H., Wu S.-J., 2013, Mod. Phys. Lett. A, 28, 1340013
Olausen S. A., Kaspi V. M., 2014, ApJS, 212, 6
Petri J., 2016, J. Plasma Phys., 82
Ruffini R., Vereshchagin G., Xue S.-S., 2010, Phys. Rept., 487, 1
Santangelo A. et al., 2019, Sci China-Phys Mech Astron, 62, 1
Schwinger J., 1951, Phys. Rev., 82, 664
Sorokin D. P., 2022, Fortschr. Phys., 70, 2200092
Spivak M., 1999, A Comprehensive Introduction to Differential Geometry, 3rd edn. A Comprehensive Introduction to Differential Geometry Vol. 2. Publish or Perish, Inc., Houston, Texas
Taverna R. et al., 2022, Science, 378, 646
Wadiasingh Z. et al., 2019, Bull. Am. Astron. Soc., 51
Wang C., Lai D., 2007, MNRAS, 377, 1095
Yoon J. W., Kim Y. G., Choi I. W., Sung J. H., Lee H. W., Lee S. K., Nam C. H., 2021, Optica, 8, 630

APPENDIX A: KINEMATIC PROPERTIES OF A TWISTED CURVE AND THE FRENET–SERRET FORMULAS

At the end of Section 3, the trajectory of our light ray has been identified as a twisted curve. Formally, kinematic properties of a twisted curve can be interpreted by means of the Frenet–Serret formulas (Spivak 1999), which are known to be

$$\frac{\mathrm{d}}{\mathrm{d}s}\begin{bmatrix}\mathbf{T}\\ \mathbf{N}\\ \mathbf{B}\end{bmatrix}=\begin{bmatrix}0 & \kappa & 0\\ -\kappa & 0 & \tau\\ 0 & -\tau & 0\end{bmatrix}\begin{bmatrix}\mathbf{T}\\ \mathbf{N}\\ \mathbf{B}\end{bmatrix}, \tag{A1}$$

where $\mathbf{T}$, $\mathbf{N}$, and $\mathbf{B}$ are named the unit tangent, normal, and bi-normal vectors, respectively, which collectively constitute the Frenet–Serret frame that forms an orthonormal basis of 3-space, s is an affine parameter to measure the arc length along the curve, κ is the curvature, and τ is the torsion of the curve. Intuitively, κ measures the failure of the curve to be a straight line, while τ measures the failure of the curve to be planar; in regard to our case, the former refers to the trajectory being deflected from a straight line as viewed in the xz-plane (due to the quantum refraction effect), while the latter refers to the trajectory following a parabolic path in another plane perpendicular to the xz-plane, hence failing to stay in a single plane (due to the rotational effect of the pulsar magnetosphere).

The Frenet–Serret analysis is available to a curve which is expressed by a well-behaved C^k function with $k \geq 3$ everywhere it is defined. However, the trajectory curve of our light ray, $\mathbf{r} = (X, Y, Z)$, as given by equations (32)–(34), is not well-defined in this sense, and therefore, we cannot resort to the Frenet–Serret formulas to construct the orthonormal basis $\{\mathbf{T}, \mathbf{N}, \mathbf{B}\}$ out of the curve. Instead, we use rather a geometrically intuitive approach: (i) first, build $\mathbf{T}$ from $\hat{\mathbf{n}}/\,|\hat{\mathbf{n}}|$ by its definition, (ii) then, build $\mathbf{N}$ by taking N_y the same as T_y and by determining the N_x and N_z from $\mathbf{N}\cdot\mathbf{T} = 0$ and $|\mathbf{N}| = 1$ (so that the curvature of the curve be defined from the deflection in the xz-plane), and (iii) lastly, build $\mathbf{B}$ from $\mathbf{T}\times\mathbf{N}$. After some tedious calculations, they are obtained as

$$\begin{aligned}\mathbf{T} &\equiv \frac{\hat{\mathbf{n}}}{|\hat{\mathbf{n}}|}\\ &\approx \left(\hat{n}_{x[0]} + \frac{\hat{n}_{z[0]}^2 - \hat{n}_{x[0]}^2}{\hat{n}_{x[0]}}\delta n_{[1]}\right)\mathbf{e}_x + \hat{n}_{y[0]}\left(1 - 2\delta n_{[1]}\right)\mathbf{e}_y + \left(\hat{n}_{z[0]} + \frac{\hat{n}_{x[0]}^2 - \hat{n}_{z[0]}^2}{\hat{n}_{z[0]}}\delta n_{[1]}\right)\mathbf{e}_z + \mathcal{O}\left(\left(\Omega r_{\mathrm{o}}/c\right)^2, {}_{[2]}\right),\end{aligned} \tag{A2}$$

$$\mathbf{N} \approx \left(\hat{n}_{z[0]} + \frac{\hat{n}_{x[0]}^2 - \hat{n}_{z[0]}^2}{\hat{n}_{z[0]}}\delta n_{[1]}\right)\mathbf{e}_x + \hat{n}_{y[0]}\left(1 - 2\delta n_{[1]}\right)\mathbf{e}_y - \left(\hat{n}_{x[0]} + \frac{\hat{n}_{z[0]}^2 - \hat{n}_{x[0]}^2}{\hat{n}_{x[0]}}\delta n_{[1]}\right)\mathbf{e}_z + \mathcal{O}\left(\left(\Omega r_{\mathrm{o}}/c\right)^2, {}_{[2]}\right), \tag{A3}$$

$$\begin{aligned}\mathbf{B} &\equiv \mathbf{T}\times\mathbf{N}\\ &\approx \hat{n}_{y[0]}\left[-\hat{n}_{x[0]} - \hat{n}_{z[0]} + \left(4\hat{n}_{x[0]} + 4\hat{n}_{z[0]} - \frac{1}{\hat{n}_{x[0]}} - \frac{1}{\hat{n}_{z[0]}}\right)\delta n_{[1]}\right]\mathbf{e}_x + \mathbf{e}_y\\ &\quad + \hat{n}_{y[0]}\left[\hat{n}_{x[0]} - \hat{n}_{z[0]} + \left(-4\hat{n}_{x[0]} + 4\hat{n}_{z[0]} + \frac{1}{\hat{n}_{x[0]}} - \frac{1}{\hat{n}_{z[0]}}\right)\delta n_{[1]}\right]\mathbf{e}_z + \mathcal{O}\left(\left(\Omega r_{\mathrm{o}}/c\right)^2, {}_{[2]}\right),\end{aligned} \tag{A4}$$

where

$$\delta n_{[1]} \approx \frac{4\eta_2 B_{\mathrm{o}}^2\left(\cos\theta_{\mathrm{o}}\hat{n}_{x[0]} - \sin\theta_{\mathrm{o}}\hat{n}_{z[0]}\right)^2 r_{\mathrm{o}}^6 s^2}{\left(3\cos^2\left(\theta_{\mathrm{o}} - \alpha\right) + 1\right)^2\left[s^2 + 2\left(\cos\theta_{\mathrm{o}}\hat{n}_{z[0]} + \sin\theta_{\mathrm{o}}\hat{n}_{x[0]}\right)r_{\mathrm{o}}s + r_{\mathrm{o}}^2\right]^4}, \tag{A5}$$

taken from equation (23) with equations (18) and (19) and $B_{\mathrm{o}} = \mu\left(3\cos^2\left(\theta_{\mathrm{o}} - \alpha\right) + 1\right)^{1/2}/r_{\mathrm{o}}^3$ substituted, and $\hat{n}_{x[0]}$, $\hat{n}_{z[0]}$, and $\hat{n}_{y[0]}$ are given by equations (15)–(17), respectively. One can easily check out $|\mathbf{T}| \approx |\mathbf{N}| \approx |\mathbf{B}| \approx 1 + \mathcal{O}\left(\left(\Omega r_{\mathrm{o}}/c\right)^2, {}_{[2]}\right)$ and $|\mathbf{T}\cdot\mathbf{N}| \approx |\mathbf{N}\cdot\mathbf{B}| \approx |\mathbf{B}\cdot\mathbf{T}| \approx 0 + \mathcal{O}\left(\left(\Omega r_{\mathrm{o}}/c\right)^2, {}_{[2]}\right)$, as desired.

Following Born et al. (1999), we can determine the curvature κ of our curve $\mathbf{r} = (X, Y, Z)$ as given by equations (32)–(34):

$$\kappa = \frac{1}{\rho} = \mathbf{N}\cdot\nabla\left(\ln n\right), \tag{A6}$$

where ρ denotes the radius of curvature and $\mathbf{N}$ refers to the unit normal vector given by equation (A3) above, and the refractive index n is given by equation (10). Similarly as in Section 4, we can work out from equation (A6),

$$\begin{aligned}\kappa &= \mathbf{N}_{[0]}\cdot\nabla\left(\delta n_{[1]}\right)\\ &\approx \frac{8\eta_2 B_{\mathrm{o}}^2\left(\cos\theta_{\mathrm{o}}\hat{n}_{x[0]} - \sin\theta_{\mathrm{o}}\hat{n}_{z[0]}\right)^2\left(\hat{n}_{x[0]}^2 - \hat{n}_{z[0]}^2\right)r_{\mathrm{o}}^6}{\left(3\cos^2\left(\theta_{\mathrm{o}} - \alpha\right) + 1\right)^2\hat{n}_{x[0]}\hat{n}_{z[0]}}\,\frac{\left[3s^2 + 2\left(\cos\theta_{\mathrm{o}}\hat{n}_{z[0]} + \sin\theta_{\mathrm{o}}\hat{n}_{x[0]}\right)r_{\mathrm{o}}s - r_{\mathrm{o}}^2\right]s}{\left[s^2 + 2\left(\cos\theta_{\mathrm{o}}\hat{n}_{z[0]} + \sin\theta_{\mathrm{o}}\hat{n}_{x[0]}\right)r_{\mathrm{o}}s + r_{\mathrm{o}}^2\right]^5},\end{aligned} \tag{A7}$$

where $\mathbf{N}_{[0]}$ denotes the unperturbed (classical) part of $\mathbf{N}$, taken from equation (A3) with all the terms of $\delta n_{[1]}$ removed, and $\delta n_{[1]}$, $\hat{n}_{x[0]}$ and $\hat{n}_{z[0]}$ are given by equations (A5), (15), and (16), respectively. Here, we see that the curvature κ is solely due to the quantum refraction effect, being led by the parameter $\eta_2 B_{\mathrm{o}}^2$. In Fig. A1(a) is plotted the curvature κ (dimensionless, multiplied by r_{o}) against $0 \leq \lambda \leq 10$ (with the substitution $s = r_{\mathrm{o}}\lambda$ in equation A7), and in Fig. A1(b) is plotted the corresponding curve $(X/r_{\mathrm{o}}, 0, Z/r_{\mathrm{o}})$, which is projected on to the xz-plane. Here, we assume $r_{\mathrm{o}} = 2 \times 10^6$ cm, $\theta_{\mathrm{o}} = 60^\circ$, $\alpha = 45^\circ$, $\Omega = 2\pi \times 10^2$ Hz, and $\eta_2 B_{\mathrm{o}}^2 \sim 10^4$ (10^9 times as large as an actual order $\sim 10^{-5}$; fairly exaggerated for intuitive visualization). Note the two points marked for $\kappa_{\min}$ and $\kappa_{\max}$ in each plot; in particular, the trajectory is curved the most downward and the most upward at the former and the latter points, respectively.

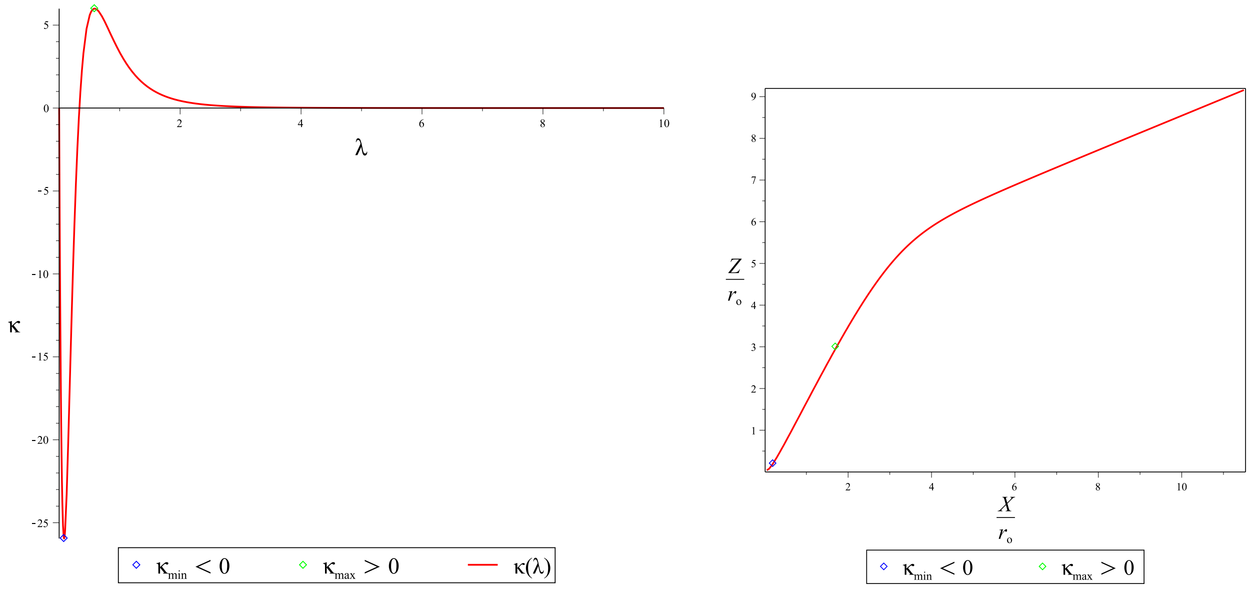

(a)

(b)

Figure A1. (a) The curvature κ (dimensionless) plotted against $0 \leq \lambda \leq 10$, (b) the curve (X/r_{o}, 0, Z/r_{o}) in the xz-plane, corresponding to the curvature κ (λ).

This paper has been typeset from a TEX/LATEX file prepared by the author.